© 2018. Published by The Company of Biologists Ltd | Journal of Cell Science (2019) 132, jcs219717. doi:10.1242/jcs.219717

RESEARCH ARTICLE

SPECIAL ISSUE: RECONSTITUTING CELL BIOLOGY

Polarity sorting drives remodeling of actin-myosin networks

Viktoria Wollrab[1], Julio M. Belmonte[2,*], Lucia Baldauf[1], Maria Leptin[2], François Nédeléc[2,‡] and Gijsje H. Koenderink[1,‡]

ABSTRACT

Cytoskeletal networks of actin filaments and myosin motors drive many dynamic cell processes. A key characteristic of these networks is their contractility. Despite intense experimental and theoretical efforts, it is not clear what mechanism favors network contraction over expansion. Recent work points to a dominant role for the nonlinear mechanical response of actin filaments, which can withstand stretching but buckle upon compression. Here, we present an alternative mechanism. We study how interactions between actin and myosin-2 at the single-filament level translate into contraction at the network scale by performing time-lapse imaging on reconstituted quasi-2D networks mimicking the cell cortex. We observe myosin end-dwelling after it runs processively along actin filaments. This leads to transport and clustering of actin filament ends and the formation of transiently stable bipolar structures. Further, we show that myosin-driven polarity sorting produces polar actin asters, which act as contractile nodes that drive contraction in crosslinked networks. Computer simulations comparing the roles of the end-dwelling mechanism and a buckling-dependent mechanism show that the relative contribution of end-dwelling contraction increases as the network mesh-size decreases.

KEY WORDS: Actin cytoskeleton, Actin-myosin contraction, Active gel, Cell cortex, Myosin end-dwelling, Polarity sorting

INTRODUCTION

Cells have the remarkable ability to actively deform themselves to drive vital processes such as cell division, cell migration and multicellular tissue dynamics. The main determinant of cell shape is the actin cytoskeleton, which actively deforms the plasma membrane by generating pushing and pulling forces (Blanchoin et al., 2014). This activity relies on the polarity of actin filaments, which have structurally distinct ends: the pointed and the barbed end, denoted also as the minus and plus end, respectively. Hydrolysis of adenosine triphosphate (ATP) bound to actin monomers that add onto the plus end of growing filaments provides chemical energy, which allows actin filaments to exert polymerization forces at their plus ends (Jégou and Romet-Lemonne, 2016). Myosin-2 motors take advantage of the structural polarity of F-actin to move in a directional manner toward the plus end, again using energy released from ATP hydrolysis (Houdusse and Sweeney, 2016). The motors work together in teams known as bipolar filaments, with motor heads on the two ends and the tails packed in the center (Liu et al., 2018). This bipolarity allows myosin filaments to slide antiparallel actin filaments in opposing directions.

Together with accessory crosslinking proteins, actin and myosin-2 form different contractile assemblies in the cell (Murrell et al., 2015). Directly underneath the plasma membrane, they form a thin and dense polymer mesh known as the cortex (Chugh and Paluch, 2018). A key property of the cortex is its contractility, which can drive global cell rounding as cells enter mitosis, local membrane constriction during cell division and global tissue deformation in developing embryos (reviewed in Chalut and Paluch, 2016). In the cytoplasm, actin and myosin form bundled contractile structures known as stress fibers in adherent cells, and 3D meshworks in large oocytes and early embryo cells (Bun et al., 2018; Field and Lénárt, 2011; Naumanen et al., 2008). Finally, during cytokinesis, actin and myosin form the cytokinetic ring, a contractile structure that constricts the membrane (Wollrab et al., 2016).

Despite detailed knowledge of the molecular composition of many actin-myosin systems (Biro et al., 2013; Zaidel-Bar et al., 2015), the molecular mechanism(s) supporting the contractile activity is unclear. The main reason is that the actomyosin bundles and meshworks in nonmuscle cells are disordered in terms of the filament orientations and polarities. This is completely unlike muscle sarcomeres, where the actin and myosin are arranged in repeating arrays, with myosin bipolar filaments localized in-between antiparallel actin filaments, having their minus ends inwards and their plus ends outwards. In this case, the localization of the myosin clusters in the vicinity of F-actin minus ends, and the anchoring of the actin filament minus ends at the Z-discs, convert the sliding activity of the motors into pure contraction (Gautel and Djinovic-Carugo, 2016). By contrast, motor-mediated sliding of rigid filaments in random networks is, in principle, equally likely to result in contraction or expansion (Kruse and Jülicher, 2000; Lenz, 2014; Mendes Pinto et al., 2012). Both contraction and expansion have indeed been demonstrated experimentally in reconstituted networks of microtubules and motors (Foster et al., 2015; Sanchez et al., 2012; Torisawa et al., 2016) and in cells (Lu et al., 2013). In contrast, actomyosin assemblies in cells are predominantly contractile, and reconstituted networks of actin filaments and myosin motors are nearly always contractile (Stam et al., 2017).

It has been a long-standing question why actin-myosin networks are biased towards contraction, and different microscopic mechanisms have been proposed (Koenderink and Paluch, 2018). The current most-favored mechanism is based on the nonlinear elastic properties of actin filaments. Actin filaments are semiflexible polymers with a persistence length of ∼10 µm (Kang et al., 2012). As a consequence, they resist stretching but readily buckle under compression forces induced by molecular motors. Theoretical models of active networks predict that buckling will cause contraction in both bundles and meshworks, independent of filament polarity (Freedman et al., 2017; Lenz et al., 2012; Ronceray et al., 2016). Myosin bipolar

[1]Department of Living Matter, AMOLF, Science Park 104, 1098 XG Amsterdam, The Netherlands. [2]EMBL, Cell Biology and Biophysics Unit, Developmental Biology Unit and Director's Research Unit, Meyerhofstraße 1, 69117 Heidelberg, Germany. *Present address: Department of Physics, NC State University, Raleigh 27695, NC, USA.

‡Authors for correspondence (g.koenderink@amolf.nl; nedelec@embl.de)

J.M.B., 0000-0002-4315-9631; M.L., 0000-0001-7097-348X; F.N., 0000-0002-8141-5288; G.H.K., 0000-0002-7823-8807

Received 6 May 2018; Accepted 1 November 2018

Journal of Cell Science (2019) 132, jcs219717. doi:10.1242/jcs.219717

filaments interacting with crosslinked actin networks therefore act as contractile force dipoles (MacKintosh and Levine, 2008). This buckling scenario is supported by direct experimental observations of filament buckling and telescopic contraction in reconstituted actin-myosin bundles and random networks (Murrell and Gardel, 2012; Linsmeier et al., 2016).

However, analytical and computational models predict that contraction can also occur in the absence of filament buckling. The rod-like shape of myosin filaments is expected to give them a tendency to rotate toward low-energy contractile configurations (Dasanayake et al., 2011). Moreover, stereospecific binding by the heads has been proposed to give rise to a mechanical anisotropy (Rubinstein and Mogilner, 2017). A further way in which motors can contract filamentous networks, irrespective of the shape of motor assemblies, is by polarity sorting. Polarity sorting is the result of a process in which motors processively walk along cytoskeletal filaments towards one end (the plus end in case of myosin-2) and dwell there before they detach; both in bundles and in networks this causes contraction (Kruse and Jülicher, 2000; Zumdieck et al., 2007; Surrey et al., 2001). In networks, a clear signature of polarity sorting is the formation of asters, radial arrays of filaments in which the filament ends point inwards and motors accumulate in the center. For microtubules, several processive motors have been shown to exhibit end-dwelling behavior (Akhmanova and Hoogenraad, 2005) and this activity has been shown to result in the formation of polar asters (Foster et al., 2015; Surrey et al., 2001; Torisawa et al., 2016; Tan et al., 2018). In the case of actin, polar asters, with actin filament plus ends pointing inwards and myosin-2 motors accumulated in the center, have been observed in systems reconstituted *in vitro* (Backouche et al., 2006; Köster et al., 2016; Soares e Silva et al., 2011; Stam et al., 2017) as well as in cells (Luo et al., 2013; Verkhovsky et al., 1997). These observations suggest that myosin-2 must be capable of sorting actin filaments by polarity. Myosin-2 bipolar filaments can indeed move processively along actin filaments under dilute conditions (Sellers and Kachar, 1990; Vogel et al., 2013). However, it has been observed that long-distance translocation of myosin filaments is suppressed in dense actin-myosin networks (Murrell and Gardel, 2014). Moreover, it is unknown whether myosin motors dwell at actin filament plus ends. The lack of direct evidence of myosin interacting with a single actin filament hinders our ability to understand the contraction of a whole network.

Here, we study how interactions between actin and myosin-2 at the single-filament level translate into contractile activity at the network scale by performing time-lapse fluorescence imaging on reconstituted quasi-2D networks of actin filaments and myosin motors. This 2D geometry mimics the quasi-2D random organization of the actin cortex and furthermore facilitates high-resolution imaging of actin-myosin interactions at the single-filament level. As actin-myosin remodeling is fast, we use an open chamber assay that allows us to capture the initial steps of myosin-mediated remodeling immediately following the addition of components that trigger contractile activity. We show that myosin-2 bipolar filaments remodel initially random actin meshworks into polar asters. Experiments at low filament densities reveal that single myosin filaments processively walk towards actin filament plus ends, where they dwell. This end-dwelling behavior allows myosin filaments to transport actin filament ends together to form asters. By observing actomyosin remodeling over a range of time and length scales, we show that the polarity sorting at the single-filament level drives aster formation and subsequent local or global network contraction, depending on the network connectivity. We use computer simulations to estimate the relative importance of myosin-mediated polarity sorting and buckling of actin filaments for contraction *in vivo*, where the filaments are shorter and the network is denser than in our experiments *in vitro*.

RESULTS

Myosin-2 bipolar filaments dwell at actin filament ends

To resolve the mechanism by which myosin-2 bipolar filaments drive remodeling of actin networks, we reconstitute 2D networks of skeletal muscle actin and myosin labeled in different fluorescent colors on nonadherent glass surfaces and observe remodeling by total internal reflection fluorescence (TIRF) microscopy. Myosin-driven remodeling is a fast process with changes in the actin network already occurring within the first few seconds. In traditional flow cells, these events would be difficult to capture. Therefore, we use an open chamber assay inspired by previous 2D contractile assays (Stam et al., 2017), which allows us to trigger remodeling by adding myosin or ATP during the time-lapse acquisition (Fig. 1A; Movie 1). When we add myosin to a pre-polymerized, random actin network, we observe that myosin starts to remodel actin as soon as it reaches the imaging surface (Fig. 1B). Within 40 s, this remodeling leads to the formation of radial arrays of actin filaments with dense myosin foci at their center, which we will refer to as asters, in line with earlier literature (Backouche et al., 2006; Köster et al., 2016; Soares e Silva et al., 2011; Stam et al., 2017). Time-lapse imaging of the trajectories of myosin thick filaments shows that they move directionally inward along the actin filaments that emanate from the center of the asters. Given that myosin-2 motors are plus-end directed, this observation suggests that the arrays are polar with actin plus ends oriented inwards (Fig. 1C,D). This interpretation is in line with earlier reconstitution studies, which likewise concluded that myosin remodels initially random actin networks into arrays of polar asters based on the inward motion of myosin on these asters (Backouche et al., 2006; Stam et al., 2017).

To further prove that myosin remodels the initially random actin network into polarity-sorted structures, we used fluorescently tagged capping protein as a plus-end marker, similar to Köster et al. (2016). We find that the actin filament plus ends accumulate in the center of the asters (Fig. 1E), demonstrating that the asters are indeed radially polar (Fig. 1F).

To understand how motors achieve polarity sorting, we used more dilute conditions in which we can observe interactions of single myosin bipolar filaments with single actin filaments. We triggered myosin activity by adding ATP to a network of pre-polymerized actin and myosin. Prior to ATP addition, the actin filaments are densely decorated with myosin thick filaments (leftmost image in Fig. 2A), which bind strongly to F-actin in the absence of ATP. The actin filaments are present in the form of bundles, likely due to the combined effect of myosin acting as crosslinkers and the presence of the crowding agent methylcellulose. Upon ATP addition, most myosin thick filaments detach from the actin filaments, consistent with the low duty ratio of myosin-2 (Harris and Warshaw, 1993). The actin bundle disassembles into single filaments, suggesting that the bundling observed before ATP addition is indeed mediated by crosslinking myosin (Movie 2). The remaining myosin filaments unidirectionally run along the actin filaments with a typical mean speed of 2 µm/s (Fig. 2B). We do not observe myosin detachment from the actin filaments unless the myosin filament encounters another actin filament, whereafter it switches track and runs along the new actin filament (after 28 s in Fig. 2A). Remarkably, as the myosin thick filament reaches the end of the actin filament, it dwells there. This can lead to an accumulation of myosin filaments if several of them run along the same actin filament (Fig. 2C; Movie 3).

Journal of Cell Science (2019) 132, jcs219717. doi:10.1242/jcs.219717

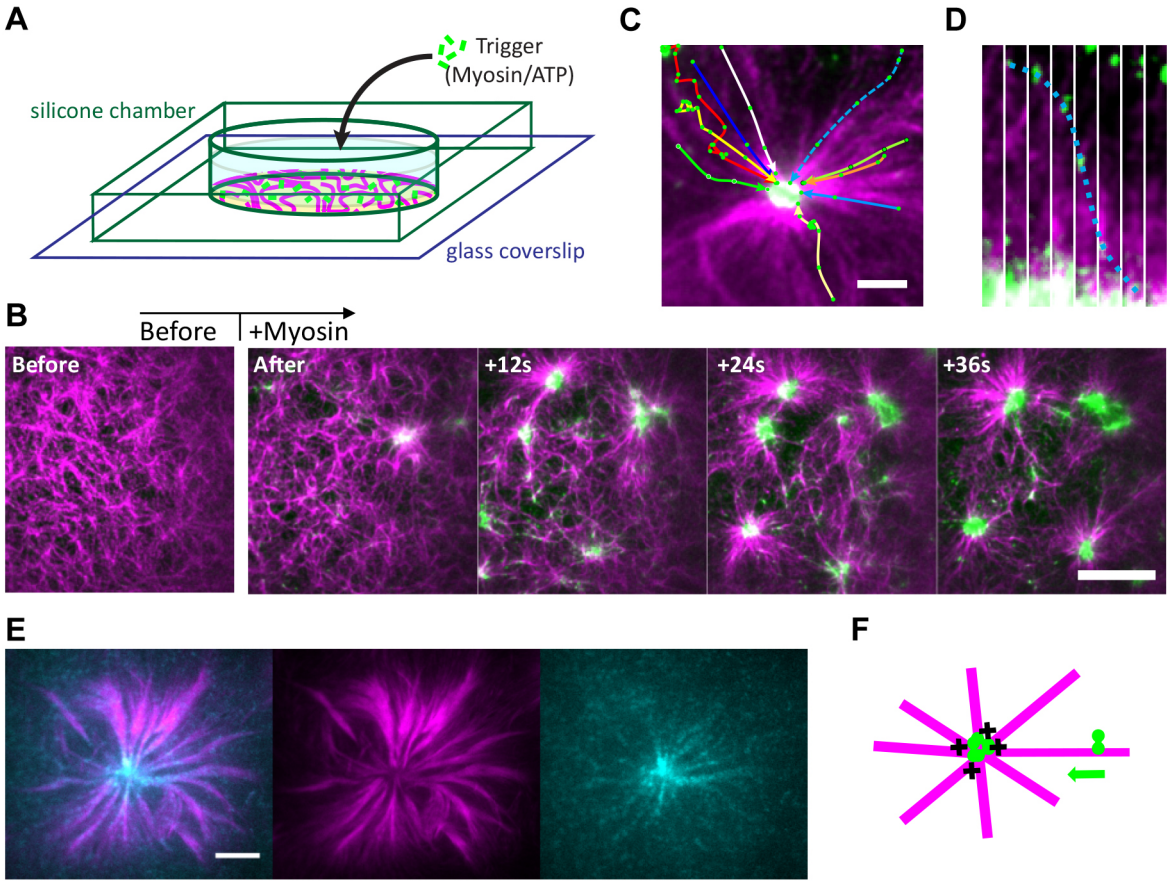

Fig. 1. Myosin-induced actin network remodeling triggered by myosin addition. (A) An open chamber allows myosin or ATP to be added while the network located near the glass bottom is observed by time-lapse TIRF. (B) The initially disordered actin network (magenta) is rapidly remodeled by myosin (green) into asters. Scale bar: 20 µm. Seconds after myosin addition are noted in the upper-left corner of the images. (C) Still image of an aster superposed with myosin trajectories (green data points connected by solid and dashed line arrows) recorded after aster formation was complete and measured over a period of 206 s. Myosins move to the center of the aster, indicating that actin filaments are polarity sorted with their plus ends oriented inwards. Scale bar: 5 µm. (D) Kymograph showing a myosin filament moving to the center of the aster. The trajectory corresponds to the blue dashed line arrow in C. Time between frames is 2 s. (E) Actin asters are polar structures with filament plus ends accumulated in their center. Capping protein (blue) is accumulated at the center of actin (magenta) asters. Scale bar: 10 µm. (F) Schematic representation of the polarity of the actin aster. Actin plus ends are in the center, minus ends are pointing outwards and myosin motors (green) accumulate at the filament plus ends in the center.

Myosin end-dwelling on single actin filament ends is a common event (Fig. 3A). This configuration is stable for at least several minutes. To determine a lower limit for the end-dwelling time, we observed myosin end-dwelling for at least 4 min. In only 6% of the cases (n=36) did myosin detach during this time. From this, we estimate a characteristic dwell time of ≃64 min, assuming a Poisson process (see Supplementary Information). We also find end-dwelling events that last over 15 min. Interestingly, myosin and actin ends seem not to overlap completely, which becomes clear when we plot line profiles of the myosin and actin intensities (Fig. 3B). By analyzing the edge positions of the filaments from many such line profiles, we infer the lengths of the myosin filaments and the overlap of the myosin and actin filament. We determine the average myosin length as 0.8 µm (Fig. 3C), in agreement with transmission electron microscopy data (Fig. S1). The average overlap of the myosin and actin filaments is ≃50% (Fig. 3C). This suggests that the ability of myosin filaments to dwell at the ends of F-actin is linked to their 'bipolarity' as depicted in Fig. 3D. This is consistent with prior reports of an interaction of F-actin with the trailing end of the bipolar myosin filament (Sellers and Kachar, 1990; Yamada and Wakabayashi, 1993).

Myosin drives clustering of actin filament ends to form asters

We then tested whether the processive motion and end-dwelling behavior of myosin can account for the formation of actin asters via polarity sorting, given that theoretical models and simulations predict that these two properties are necessary and sufficient (Freedman et al., 2017; Kruse and Jülicher, 2000; Nédélec et al., 1997; Surrey et al., 2001; Zumdieck et al., 2007). We therefore increased the actin filament concentration so that filaments overlap (see Table S1 for details). We again observe that end-dwelling is a common event (Fig. S2, yellow dashed line circles). Furthermore, we see many examples of myosin connecting filament ends, forming incipient asters (Fig. S2, cyan dashed line circles). To understand the formation of these structures, we turned to live imaging. We see that myosin that is already bound to the end of one actin filament can still processively run along another actin filament (Fig. 4A; Movie 4). As it arrives at the other filament's end, it dwells there and thereby holds the filament ends together. These bipolar structures can grow further and catch additional actin filaments (Fig. S3). This type of behavior illustrates a mechanism that transports filament ends toward each other, as depicted in Fig. 4B. At concentrations of filaments and myosin used in this assay, the incipient aster configurations are not stable. Myosin can

Journal of Cell Science (2019) 132, jcs219717. doi:10.1242/jcs.219717

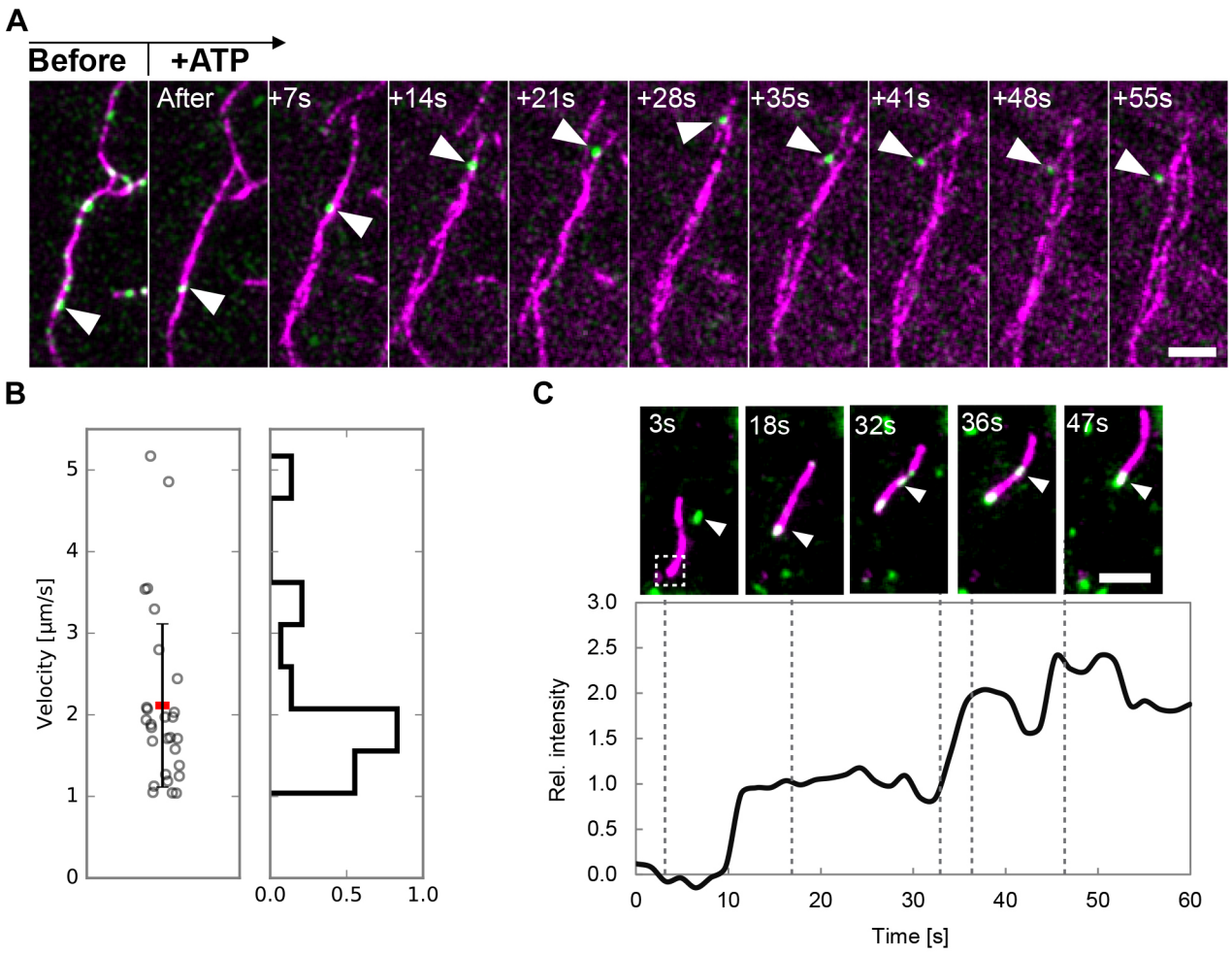

Fig. 2. Myosin-actin interaction at low filament concentration. (A) Before ATP is added (leftmost image), myosin binds to actin and is immobile. Note that the actin filaments are bundled by the strongly bound myosins. Upon addition of ATP, most myosin filaments detach and the bundle dissolves; one remaining myosin filament (arrowheads) runs along an actin filament, switches track as it encounters another actin filament at 28 s, and runs on the new filament until it reaches the end and dwells there. Scale bar: 5 µm. (B) Left: velocities of myosins running along actin. Every data point corresponds to one myosin trajectory (a total of 28 trajectories obtained in eight independent experiments). The horizontal red bar indicates the mean value (2 µm/s) and the error bar the s.d. (1 µm/s). Right: distribution of velocities. The velocity was only measured while myosin was moving. (C) Myosin accumulation at actin filament ends. Top: three myosin filaments (arrowheads) bind to an actin filament and move to the end. Bottom: increase in fluorescence (Alexa Fluor 488) at the end of the actin filament (measured in the region indicated by the dashed line box in the leftmost image above). The intensity is normalized to the intensity of the first myosin filament that reaches the actin end. Scale bar: 5 µm.

detach from one of the filaments while staying attached to the other (Fig. 4A, rightmost image). We used higher actin filament concentrations to test whether this mechanism is also active in dense networks (Fig. 4C; Movie 5). We see the same mechanism: as myosin runs along one filament (cyan), it encounters a second filament (yellow). Subsequently, it moves on both filaments and stops when it arrives at the two filament ends. This configuration is stable for a few minutes until myosin switches to another filament and starts to move on that one (Fig. 4C, rightmost image). These observations show that myosin end-dwelling and processive motion permit the transport of filament ends towards each other, gathering them for some time, and thereby induce polarity sorting. We note that under the conditions reported in Fig. 4, we did not observe any examples of actin filament buckling.

We next tested whether polar structures are also present at the higher actin densities used in prior reconstitution studies of contractility in actin-myosin networks (Murrell and Gardel, 2012, 2014; Schuppler et al., 2016; Vogel et al., 2013). Time-lapse imaging shows that asters still form at higher actin densities (Fig. 5A; Movie 6). Because asters are polar, they should, in principle, be able to merge due to the action of myosin motors. We indeed observe that neighboring asters interact. An example is shown in Fig. 5B,C: here, two adjacent asters move toward one another and eventually merge. We occasionally observe events when asters split into two smaller asters (Fig. 5D). Aster splitting could be linked to the ability of myosin filaments to detach from actin filament ends when they have the option to switch to another actin filament, as we observed at low filament densities. Consistent with this idea, we also observe exchange of myosin between asters (Fig. 5E).

Crosslinking promotes long-range aster interactions and network contraction

In vitro studies (Alvarado et al., 2013; Bendix et al., 2008; Ding et al., 2017; Ennomani et al., 2016; Koenderink et al., 2009; Köhler et al., 2011; Murrell and Gardel, 2012; Stam et al., 2017) and observations in cells in which crosslinkers were depleted (Ding et al., 2017) have shown that crosslinkers promote long-range

Journal of Cell Science (2019) 132, jcs219717. doi:10.1242/jcs.219717

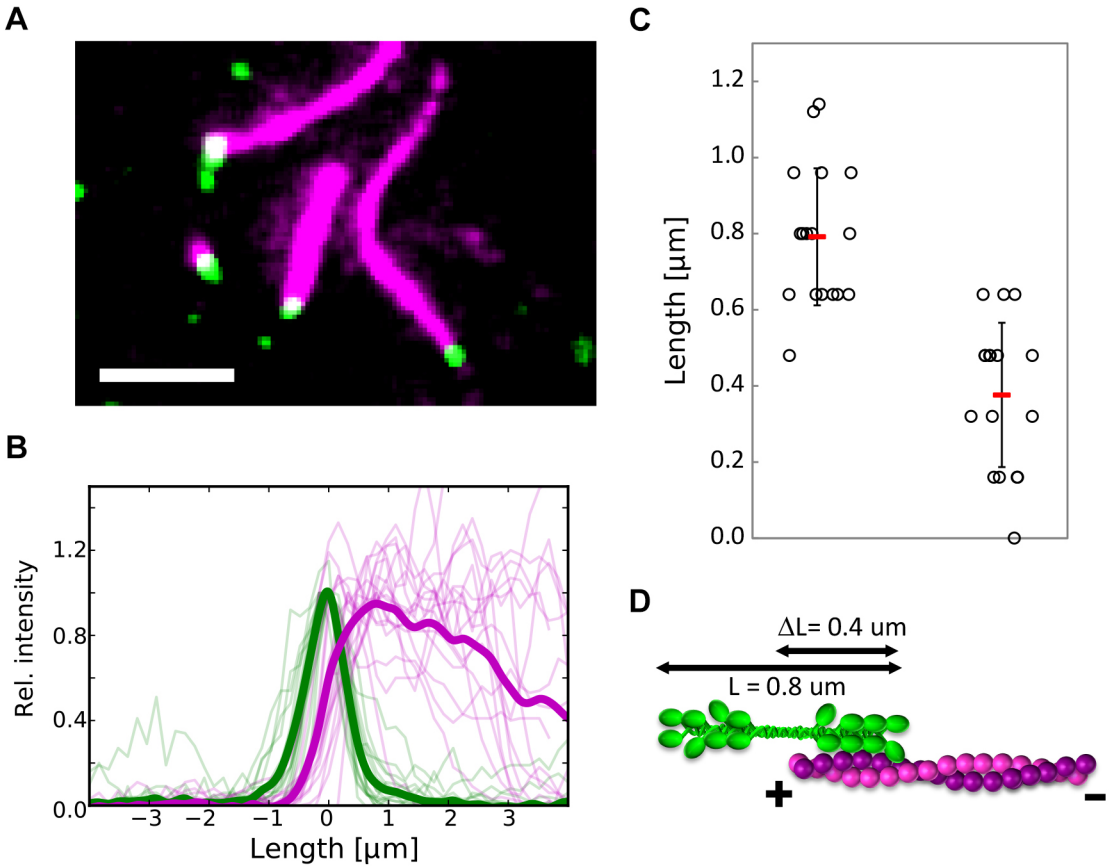

Fig. 3. Position of myosin at actin filament ends. (A) Examples of myosin (green) dwelling on actin (magenta) filament ends. Scale bar: 5 µm. (B) Intensity line profiles of actin and myosin for 17 events (thin lines). Pairs of actin and myosin profiles are aligned with respect to the myosin peak intensity. The intensities are normalized to the peak intensity for each profile. Thick lines show the average profiles. (C) From the intensity line profiles, we determine the position of the edges of the myosin filaments and the actin filament by taking the first derivative of the signal. We thus extract an average myosin filament length of 0.8±0.2 µm (left) and an average overlap between end-dwelling myosin and actin filaments of 0.4±0.2 µm (right); red bars indicate the mean values, error bars the s.d. (D) Schematic representation of myosin end-dwelling. As myosin only overlaps by about half of its total length, we suggest that the trailing end is involved in end-dwelling.

contraction. Indeed recent theoretical models predict that crosslinkers should promote motor-driven network contraction above a percolation threshold (Ennomani et al., 2016; Sheinman et al., 2015). Consistent with those studies, when we add the crosslinking protein α-actinin-1 (Ciobanasu et al., 2014), we observe that the asters are larger, persistently move towards each other over distances of tens of µm and invariably merge (Fig. 5F–H; Movie 7). The fusion of two aster cores can be also observed when we label the core of the asters with fluorescent capping protein, which marks the actin filament plus ends (Fig. 5I). Long-range force transmission is mediated by α-actinin-1-rich actin bundles, which connect the asters (Fig. S4). In addition to growing by merging, asters can also grow by a radial inward flow of actin filaments and myosin along the aster arms (Fig. S5, Movie 8). We conclude that crosslinkers favor contraction not only by providing elastic connections, but also by allowing the formation of stable F-actin bundle tracks that promote inward transport of myosin to form stable asters. Moreover, they form stable connections of mixed polarity between asters, stimulating aster merging (depicted in Fig. 5J).

We tested how polarity sorting influences network contraction on large scales. As reported previously (Alvarado et al., 2013; Belmonte et al., 2017; Bendix et al., 2008), the balance between crosslinking and motor activity determines the contractile behavior of actin-myosin networks. We fixed the α-actinin-1 concentration at a molar ratio with actin of R_C=1:50, which is well above the percolation threshold for 2D networks (Alvarado et al., 2017). To explore different regimes, we varied the myosin concentration. We confined actin-myosin networks containing 0.1 mM ATP in large 2 mm × 22 mm chambers with nonadhesive walls, and imaged the entire network over time from the point at which contractility is triggered by mixing actin and myosin in the presence of ATP. Starting with a high myosin-to-actin ratio, R_M=0.05, we find network contraction only on short length scales (Fig. 6A, magenta; Movie 9). Looking at the dense actin-myosin clusters at higher magnification, we find that they are composed of actin asters with myosin foci at their core (Fig. 6B, magenta). As we decrease R_M to 0.01, we still find actin asters, but, in this condition, they are embedded in a fully percolated network. The full percolation is shown by a global network contraction (Fig. 6A). At higher magnification, we observe that the network is again made of asters (Fig. 6B). Decreasing R_M even further to 0.005 leads to stalled networks that are unable to contract (Fig. 6A, blue). Also, here we observe asters at higher magnification (Fig. 6B). We suggest that two mechanisms contribute to the contraction process. First, myosin accumulates in the center of the aster and is therefore depleted in the other areas, which do not experience major remodeling anymore. Second, aster-associated filaments have to overlap to promote the fusion of the asters. These connections are more stable for lower myosin concentrations. As schematically depicted in Fig. 6C, our experimental results suggest that aster formation contributes to both local and global contraction.

Journal of Cell Science (2019) 132, jcs219717. doi:10.1242/jcs.219717

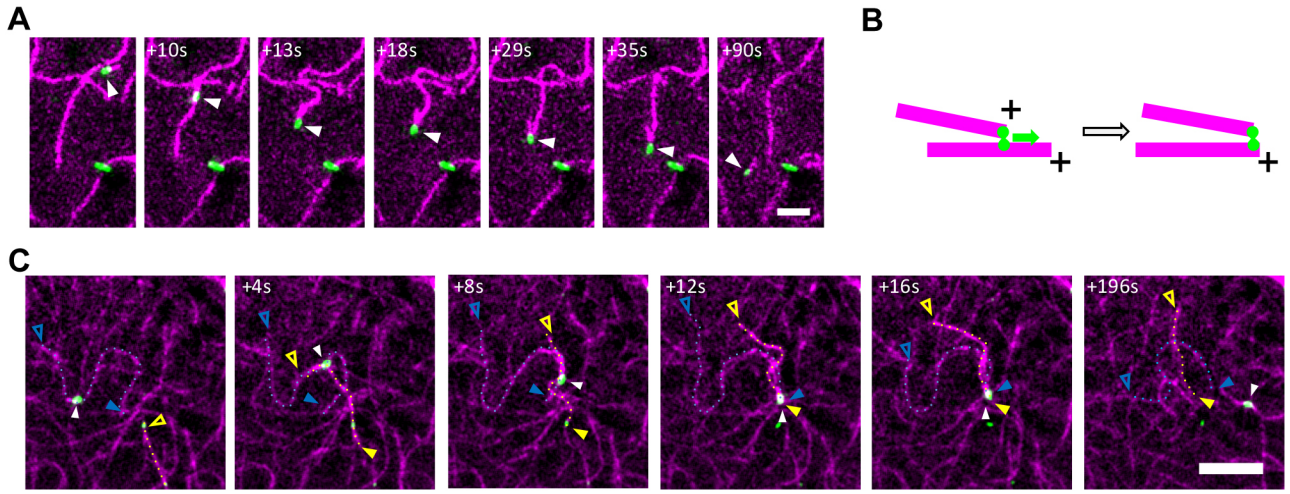

Fig. 4. Myosin motility and end-dwelling as a mechanism for polarity sorting. (A) Incipient asters forming in networks at an actin concentration of 0.12 µM, which is high enough such that filaments encounter each other pair-wise but not yet high enough to lead to dense meshworks. Myosin (white arrowheads) attached to a short actin filament at *t*=0 encounters another actin filament at 10 s and runs along it while staying attached to the first one, keeping the two filament ends together until it detaches from one at 83 s. Scale bar: 5 µm. (B) Schematic representation of the process of myosin-driven polarity sorting. Dwelling on one filament end, myosin transports the plus end as it runs along another filament and eventually joins the two plus ends. (C) Aster formation in networks with higher numbers of filaments. Myosin (white arrowheads) runs along a filament (blue arrowheads and dotted lines), encounters a second filament (yellow arrowheads and dotted lines) and moves along both filaments, joining their plus ends. This configuration is stable for several tens of seconds. Scale bar: 10 µm. Filled/empty arrowheads indicate plus/minus ends.

Simulations reveal conditions favoring different contractile mechanisms

A passive crosslinker and a motor acting together on the same filament constitute the elementary configuration of the buckling mechanism (Belmonte et al., 2017). Thus, in addition to helping the polarity-sorting mechanism, adding α-actinin-1 can promote the buckling mechanism as well. From the experimentally observed contractions, it is impossible to tell whether the polarity-sorting mechanism and the buckling mechanism are both contributing or one is dominant (Dasanayake et al., 2011; Lenz et al., 2012; Ronceray et al., 2016). We can also not judge from our *in vitro* experiments to what extent the polarity-sorting mode of contraction depends on mesh size, and may therefore play a role in physiological conditions, in which both the filaments and mesh sizes are much smaller (Bovellan et al., 2014; Eghiaian et al., 2015; Fritzsche et al., 2016; Fujiwara et al., 2016). We thus turned to computer simulations of actin networks with the software Cytosim (Nédélec and Foethke, 2007), which allows us to analyze the relative contributions of end-dwelling and buckling mechanisms in networks of different densities with filaments of different length.

In Cytosim, we modeled individual actin filaments, myosin minifilaments and α-actinin-1 crosslinkers as described in the Materials and Methods section (for details see Table S2). Although Cytosim has been used in the past to study both the buckling mechanism (Belmonte et al., 2017) and the polarity mechanism (Surrey et al., 2001) independently from each other, the current assumption is that both mechanisms can operate in concert. Polarity sorting depends on the ability of the motors to end-dwell but does not require crosslinkers. By contrast, theoretical modeling has shown that buckling-mediated contraction requires crosslinkers (Belmonte et al., 2017), or at least motors of different speeds (Lenz et al., 2012), but operates even if the motors do not end-dwell. With simulations, we can enable or disable end-dwelling and add or remove crosslinkers to assess the influence of the two mechanisms. We first modeled contraction of actin networks with myosin filaments but no crosslinkers. If we allow myosin heads to end-dwell, the network organizes into polar asters (Fig. 7A; Movie 10), with the plus ends facing inwards (Fig. 7A, rightmost image), resembling the asters observed *in vitro* (Fig. 1). If we let the motors instead detach immediately upon reaching the end of actin filaments, the network fails to contract (Fig. 7B; Movie 11). These results confirm that end-dwelling is important for driving contractility in noncrosslinked conditions, consistent with the experimental observations for *in vitro* networks.

We next added crosslinkers modeled according to the properties of α-actinin-1, and systematically varied the concentration of myosin and crosslinker (Fig. 7C; Movie 12). We observe all three network behaviors seen in the *in vitro* experiments: (1) slow or stalled networks, for high concentrations of crosslinker and low concentrations of myosin; (2) globally contracted networks, for high myosin concentrations; and (3) locally contracted asters, for low myosin and crosslinker concentrations. To assess the contribution of polarity sorting to the contraction of the networks, we repeated the simulations with the end-dwelling disabled (Fig. 7D; Movie 13). In this scenario, most of the networks fail to contract, indicating a dominant role of polarity sorting in these networks. The region of the phase diagram least affected by the absence of end-dwelling is characterized by high concentrations of crosslinkers, a condition that is crucial in the filament-buckling mechanism, as shown previously by theory, simulations and *in vitro* experiments (Belmonte et al., 2017; Freedman et al., 2018; Lenz et al., 2012; Linsmeier et al., 2016; Murrell and Gardel, 2012; Stam et al., 2017). For buckling to happen, the crosslinking density must be high enough to sustain the forces exerted by the myosin motors while buckling the filaments. Therefore, we expect the boundary between regions dominated by the filament buckling mechanism versus the polarity sorting mechanism to be determined by the ratio of end-dwelling myosins to crosslinkers. On the diagrams in which the two concentrations are varied, the regions dominated by the two mechanisms are indeed separated by a diagonal (Fig. 7C,D). We emphasize that polarity sorting and filament buckling are not mutually exclusive, as we observe both mechanisms when end-dwelling is enabled.

Journal of Cell Science (2019) 132, jcs219717. doi:10.1242/jcs.219717

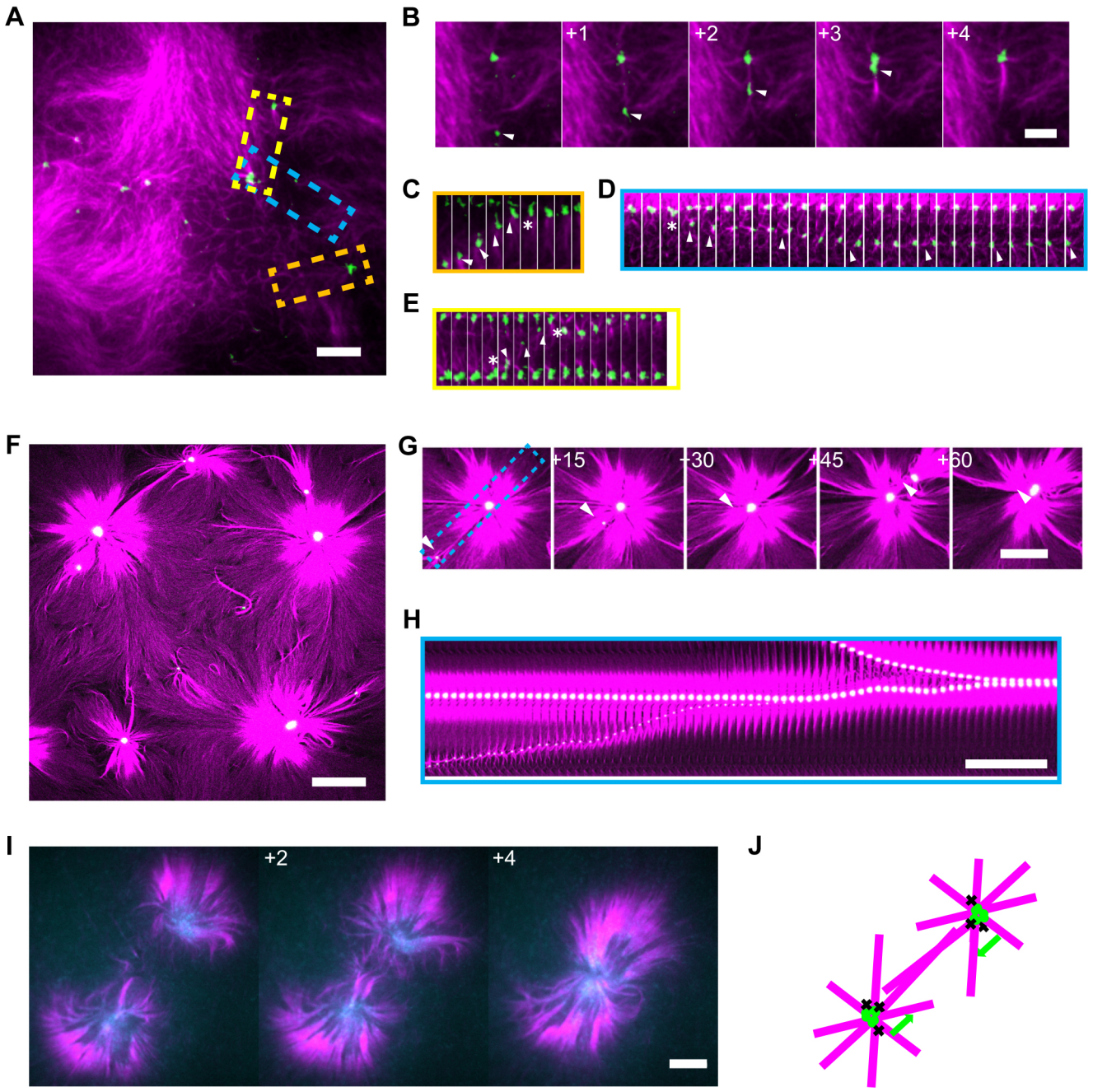

Fig. 5. Effect of α-actinin-1 on myosin-mediated actin network remodeling. (A) In the absence of α-actinin-1, myosin (green) forms small actin asters (magenta). The corresponding video is Movie 6. Scale bar: 10 µm. The dashed line boxes correspond to the kymographs outlined in corresponding colors in C–E. (B) Two asters merging (arrowheads). Asters are smaller than in crosslinked networks and show faster dynamics. Time in seconds. Scale bar: 5 µm. (C–E) Kymographs show that myosins join (C), leave (D) and get exchanged between asters (E) on second time scales. Time between frames=1 s. Arrowheads indicate the myosin position; asterisks mark the moment when myosin joins or leaves the aster. (F) In the presence of α-actinin-1 (R_C=0.01), myosin remodels actin into large asters. The corresponding video is Movie 7. Scale bar: 50 µm. (G) Two subsequent events when neighboring asters move towards each other in a persistent manner and eventually join. Time in minutes. Scale bar: 50 µm. (H) Kymograph along the dashed line box in G. Scale bar: 10 min. (I) Dual-color imaging shows that merging actin asters (magenta) are polar, with the actin filament plus ends located in the center of the asters. Plus ends are labeled with capping protein (blue). Time in minutes. Scale bar: 10 µm. (J) Schematic showing how neighboring asters move towards each other due to their polar nature.

The above results highlight the prominent role of polarity sorting in the contraction of networks that resemble the *in vitro* conditions reported in our experiments. In physiological conditions – for example, in the cortex of animal cells – the actin filaments are about one order of magnitude shorter than those in our *in vitro* systems [~1 µm or less (Fritzsche et al., 2016)], and the mesh size is also much smaller [between 0.03 µm and 0.1 µm (Bovellan et al., 2014; Fujiwara et al., 2016)]. One can thus expect polarity sorting to be even more crucial in the cortex for two reasons: first, the force required to buckle a filament segment increases with the inverse of the squared length of the segment, and thus becomes greater as the mesh size is reduced. Second, the ratio of end-dwelling versus side-bound motors also increases as the filaments become shorter. To assess these effects, we performed simulations with denser networks made of shorter

Journal of Cell Science (2019) 132, jcs219717. doi:10.1242/jcs.219717

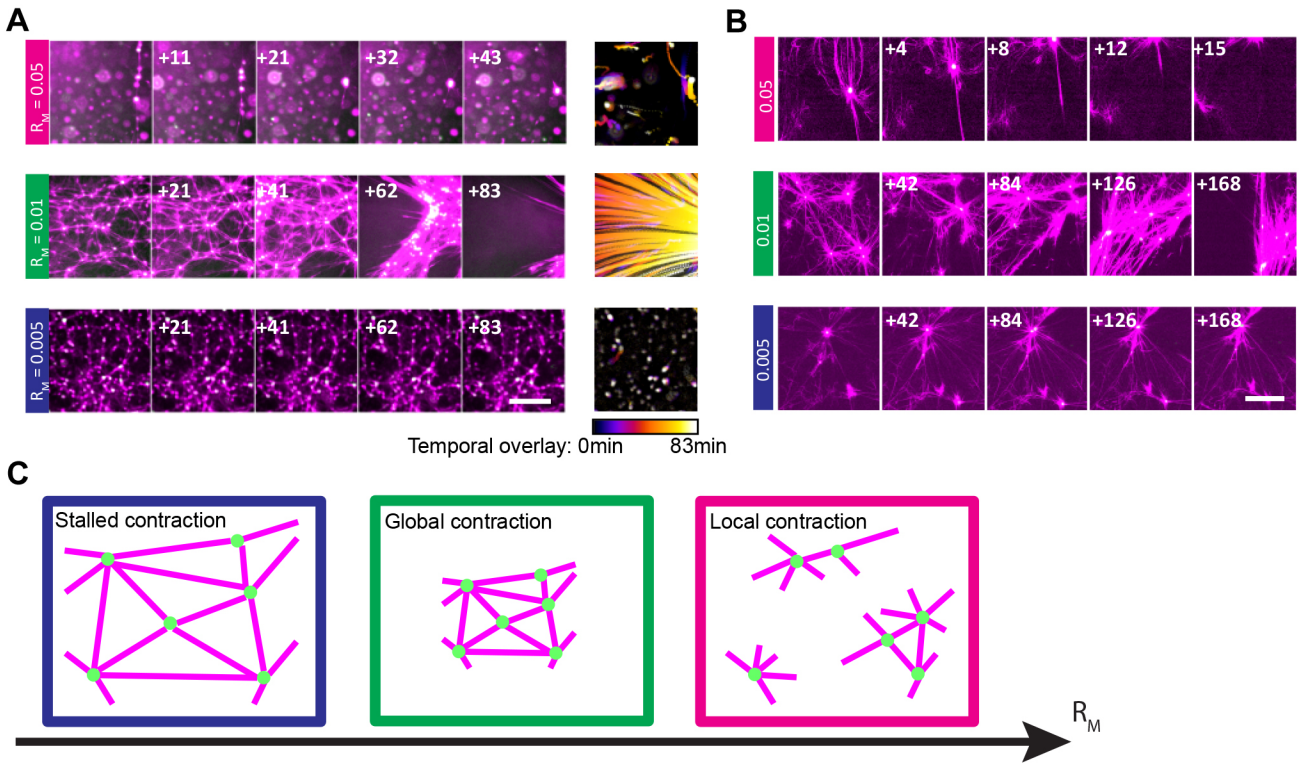

Fig. 6. Asters formed at different motor:actin concentration ratios, R_M. (A) At R_M=0.05, asters form and locally contract the network. For R_M=0.01, asters form and become part of a percolating network that exhibits global contraction. For R_M=0.005, the network is stalled and does not contract, although asters are still present. Time in minutes. Scale bar: 200 µm. (B) Higher magnification images show that asters are formed in the three regimes. Time in minutes. Scale bar: 50 µm. (C) Schematic representation of the three contraction regimes as a function of R_M.

filaments that better resemble the actomyosin cortex, and varied the concentrations of myosin and crosslinker as before (Fig. 8A; Movie 14). With these conditions, most of the networks contract to a single aster rather than multiple ones, probably because they are more tightly connected. When the end-dwelling property of myosin is disabled, the contractile behavior is lost in a region of the phase diagram (Fig. 8B; Movie 15). This region corresponds roughly to the region in which contraction was dependent on end-dwelling in the simulations with conditions chosen to mimic the *in vitro* experiments, i.e. larger mesh sizes and longer filaments (Fig. 7C,D). However, networks in the region with low myosin and high crosslinker concentrations are now stalled, whereas they were contractile under the buckling mechanism at lower density. Therefore, in the denser networks, the effectiveness of the buckling mechanism is reduced, while contraction through polarity sorting is preserved. Note that for low crosslinker concentrations, filaments freely glide over the network, powered by the myosin motors (see Movie 15 for an example). When the simulation space is only a few times larger than the filament length, the filaments are easily pushed across the simulation space, slowing down only as they reach its edges, where the network is less dense. This effect only occurs without crosslinkers and is more pronounced in Fig. 8 than in Fig. 7. These results confirm that the polarity-sorting mechanism remains effective when the actomyosin network is denser and made of shorter filaments, and overall resembles a real cortex better, while in these conditions the buckling-mediated mechanism decreases in importance.

DISCUSSION

An important biological function of actin-myosin networks is to provide contractility, and although multiple mechanisms for contraction have been identified, their relative contributions are still not understood. Here, we show that myosin motors remodel initially random actin networks into polarized domains. Using low protein densities to observe actin-myosin interactions at the single-filament level, we found a property necessary for polarity sorting: myosin dwells at actin filament ends. With this key property, contractile nodes, which are often assumed in theoretical studies of actin-myosin networks, form by self-organization (Alvarado et al., 2013; Hannezo et al., 2015; Jülicher et al., 2007; Salbreux et al., 2009). Our results corroborate earlier observations of myosin-mediated formation of polar asters in reconstituted actin-myosin networks (Backouche et al., 2006; Köster et al., 2016; Stam et al., 2017). We find that aster formation occurs over a wide range of crosslinker and myosin densities. At crosslink densities that are below the percolation threshold, the asters are small and transient. At crosslink densities above the percolation threshold, the asters are stabilized, and neighboring asters pull on each other over long distances and merge, leading to large-scale contraction. The crucial role of crosslinkers in tuning the range of force transmission is in line with other experimental studies (Alvarado et al., 2013; Bendix et al., 2008; Chugh et al., 2017; Vavylonis et al., 2008), and is predicted theoretically on the basis of a percolation transition (Ennomani et al., 2016; Sharma et al., 2016). However, we find that crosslinkers favor contraction not only by providing elastic connections, but also by allowing the formation of stable F-actin bundle tracks that promote inward transport of myosin to form large and stable asters. By contrast, in the absence of crosslinkers, myosin clusters are dynamic and split because myosin filaments can switch between different actin filament tracks. Asters are also observed over a range of motor densities, in conditions of stalled networks

Journal of Cell Science (2019) 132, jcs219717. doi:10.1242/jcs.219717

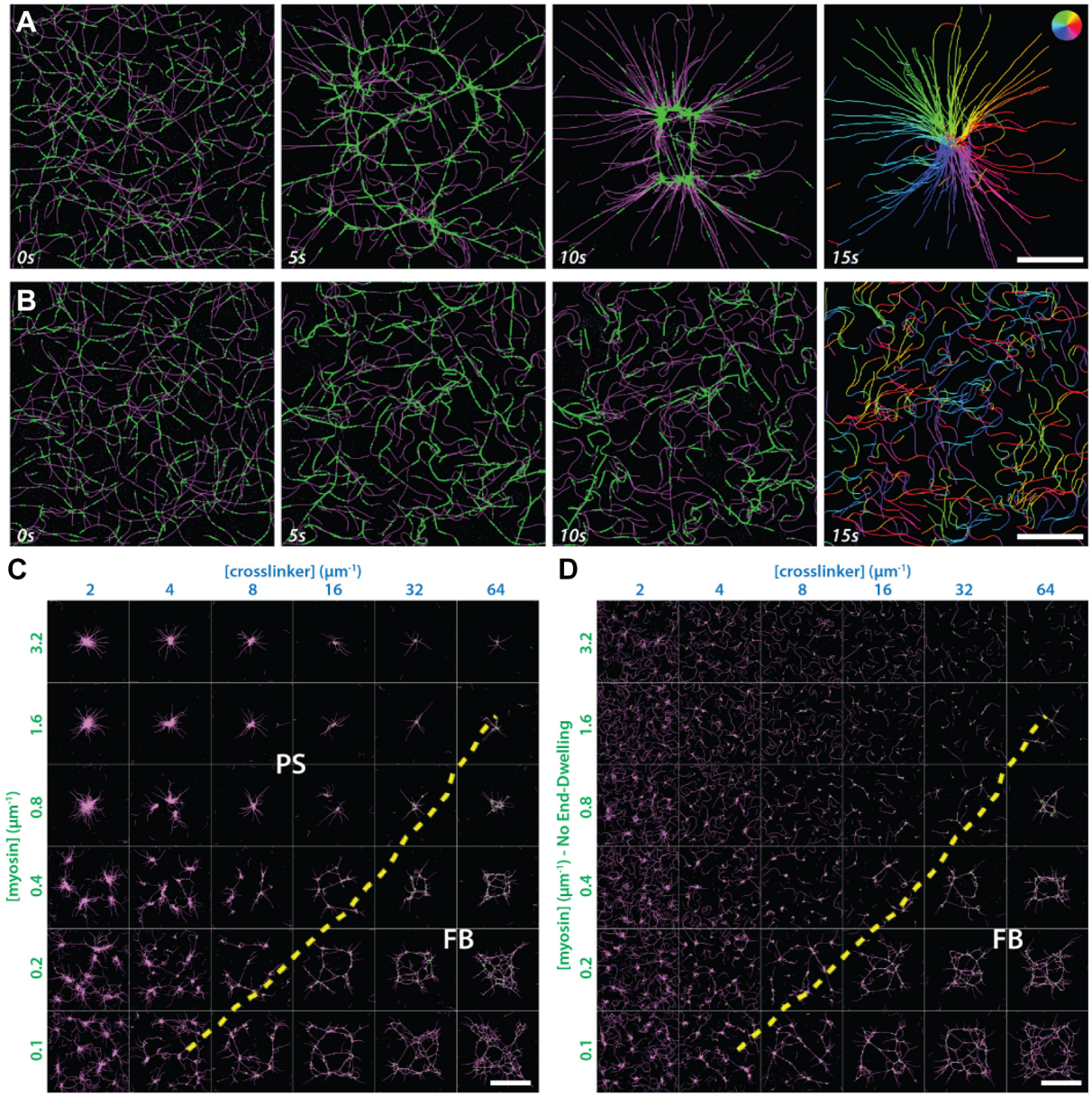

Fig. 7. Role of end-dwelling in simulated networks with parameters corresponding to *in vitro* experimental conditions. (A,B) Time series of simulations with 200 flexible filaments (actin, magenta), with average lengths of 10 µm, and myosin minifilaments (green). Myosin motors are plus-end directed and modeled with (A) or without (B) end-dwelling. The last time point shows actin filament segments colored according to their orientation (see color wheel inset). In A, asters form with all filament plus ends at the center of the aster as a result of the polarity-sorting mechanism. Without end-dwelling (B), the network does not contract. Scale bars: 10 µm. (C,D) Phase diagrams of simulated networks after 200 s of simulation with varying concentrations of crosslinkers and myosins with (C) or without (D) end-dwelling motors. Concentrations of crosslinkers and myosins are given as molecules per µm of actin filament. Actin filament lengths as in A and B, with mesh-size of 1.1 µm. In the region above the dashed yellow lines, contraction is dominated by polarity sorting (PS), as shown by the fact that contraction is lost without myosin end-dwelling. In the region below, contraction persists, also without myosin end-dwelling, showing that it is mediated by filament buckling (FB). Scale bars: 40 µm.

(low motor density), globally contracting networks (intermediate motor density) and local contraction (high motor density). These contractile behaviors are reproduced in simulations, where we can directly compare the remodeling effect of motors with and without end-dwelling. The simulations demonstrate that end-dwelling makes an important contribution to network contraction, while contraction due to filament buckling only happens for a limited set of parameters.

In our study, we use skeletal muscle myosin-2 filaments. Although muscle myosin is used in nearly all reconstituted actomyosin systems thus far, with few exceptions (Thoresen et al., 2013), contraction in nonmuscle cells is driven by nonmuscle myosins. These differ from skeletal muscle myosin-2 in their kinetic properties and the formation of much smaller bipolar filament ensembles of only 10–20 motors (Erdmann et al., 2016; Melli et al., 2017). Clearly, in the future, it will be interesting to study whether end-dwelling is also observed for nonmuscle myosin. Our results suggest that the dwelling behavior is mainly mediated by the trailing end of the myosin filaments. Although nonmuscle myosin filaments are reported to be much shorter than skeletal muscle myosin filaments (Billington et al., 2013), their higher duty ratio might compensate and still permit end-dwelling (Kovács et al., 2003;

Journal of Cell Science (2019) 132, jcs219717. doi:10.1242/jcs.219717

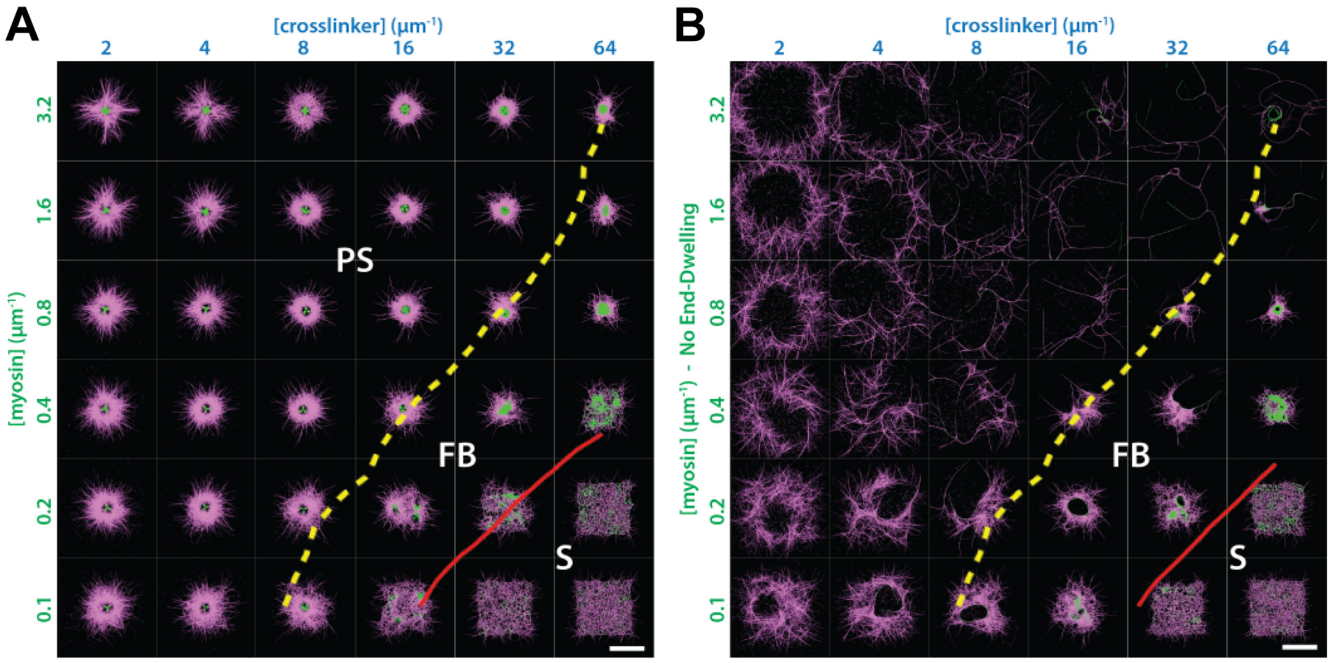

Fig. 8. Role of end-dwelling in simulated networks with parameters corresponding to the actin cortex *in vivo*. (A,B) Phase diagrams of simulated networks after 80 s of simulation with average actin filament lengths of 1 µm, mesh size of 0.1 µm and varying concentrations of crosslinkers and myosins with (A) and without (B) end-dwelling motors. Concentrations of crosslinkers and myosins are given as molecules per µm of actin filament. Dashed yellow lines demarcate the regions where contraction is dominated by polarity sorting (PS) or filament buckling (FB), as described in Fig. 7. Solid red lines indicate the boundaries between contractile and stalled (S) regions in each phase diagram. Scale bars: 4 µm. Note that the cross-like configurations in A are a reflection of the initial configuration of the network, where all filaments are placed inside a square box with open boundaries.

Wang et al., 2003). Possibly the ratio between the two major nonmuscle myosin isoforms, NMMIIA and NMMIIB (also known as MYH9 and MYH10, respectively), could also play a role in regulating filament end-dwelling (Melli et al., 2017).

Our experimental and computational findings show that myosin-driven polarity sorting can be an efficient mechanism for actomyosin network contraction, provided that enough crosslinkers are present to allow force transmission. Prior *in vitro* and *in silico* studies of reconstituted actin-myosin networks showed that, in the presence of crosslinkers, motor-mediated buckling of actin filaments can provide the dominant mechanism for contraction, sometimes augmented by the severing of buckled actin filaments (Li et al., 2018; Murrell and Gardel, 2012). However, both our experimental and computational findings suggest that, even in crosslinked networks, there is still an underlying tendency for actin and myosin to form polarity-sorted structures. The relative contributions of polarity sorting versus buckling to the overall network contraction depend on parameters such as the distance between crosslinks, the motor density and whether actin filaments are bundled. A full characterization of these parameters is beyond the scope of this study, but simple scaling considerations indicate that buckling might be disfavored *in vivo*. First, recent work suggests that the actin cortex is composed of filaments that are relatively short, being a mixture of formin-nucleated filaments with lengths on the order of 1 µm, and Arp2/3-nucleated filaments in the 100 nm range (Fritzsche et al., 2016). Second, electron microscopy images revealed typical cortical mesh sizes of only 30–200 nm, which might correspond to the distance between crosslinkers (Bovellan et al., 2014; Fujiwara et al., 2016). These characteristics would make buckling difficult, but leave polarity sorting as a potent contraction mechanism, as indicated by our simulations of dense networks of short filaments (Fig. 8).

Polarity-sorted actin structures were seen *in vivo* by electron microscopy (Begg et al., 1978; Cramer et al., 1997; Kamasaki et al., 2007; Sanger and Sanger, 1980). Furthermore, myosin foci are commonly observed in the actin cortex of cells and early embryos (Martin et al., 2009; Mayer et al., 2010; Munjal et al., 2015). However, the cell cortex is mainly regarded as a random actin network (Chugh et al., 2017). Recent theoretical studies of contractile networks with actin turnover suggest that the absence of asters in the cell cortex could be due to turnover (Guthardt Torres et al., 2010; McFadden et al., 2017). Consistent with this idea, asters can be formed in the actin cortex if actin polymerization is reduced or blocked by drugs (Luo et al., 2013; Verkhovsky et al., 1997), and actin stabilization seems to have a similar effect (Wehland et al., 1977). We therefore speculate that polarity sorting may occur in cortical actin networks but that actin turnover prevents formation of large polar domains. Moreover, polarity sorting can be counteracted by other remodeling processes, such as Arp2/3 nucleator-dependent self-organization (Fritzsche et al., 2017) and biochemical feedback between active RhoA and myosin (Nishikawa et al., 2017). New developments in high-resolution microscopy will hopefully enable the visualization of local accumulation of actin plus ends in the cortex or other contractile structures, such as the cytokinetic ring, and thereby lead to a better understanding of the role of polarity sorting in cells (Hu et al., 2017).

MATERIALS AND METHODS

Protein preparation

Actin and myosin were purified from rabbit muscle as described previously (Alvarado and Koenderink, 2015). Myosin was labeled with Alexa Fluor 488 NHS ester (Invitrogen); actin was labeled with Alexa Fluor 649 carboxylic acid, succinimidyl ester. The crosslinker protein α-actinin-1, both in unlabeled form and tagged with mCherry, was purified as described in Ciobanasu et al.

(2014). Capping protein (CP) was purified as described (Burke et al., 2017), with minor modifications. From the elution buffer, the protein was dialyzed into phosphate-buffered saline (PBS) and labeled with SNAP-surface Alexa Fluor 647 following the manufacturer's protocol (New England Biolabs). Excess dye was removed by dialyzing overnight against CP buffer [10 mM Tris-HCl pH 7.5, 40 mM KCl, 0.5 mM dithiothreitol (DTT)]. Myosin was stored in myosin buffer (300 mM KCl, 4 mM $MgCl_2$, 20 mM imidazole, 1 mM DTT) with 50% glycerol. Prior to experiments, myosin was dialyzed overnight against the myosin buffer to remove the glycerol. The high ionic strength of this buffer prevents the self-assembly of myosin into bipolar filaments. Actin was stored in G-buffer (2 mM Tris-HCl, 0.2 mM ATP, 0.2 mM $CaCl_2$, 0.2 mM DTT) in its monomeric (G-actin) form.

Chamber preparation

Glass coverslips were cleaned with base piranha for 10 min and thoroughly rinsed with MilliQ water following a published procedure (Alvarado and Koenderink, 2015). A custom-made silicone sheet with 9 mm^2 holes was placed on top of the glass coverslip to build open chambers. In some experiments (see Table S1), classical flow cells were used, similar to the ones described in Alvarado and Koenderink (2015). The surfaces were passivated with lipid bilayers: small unilamellar vesicles (SUVs, see below) were flushed into the chamber. After an incubation time of at least 5 min, excess vesicles were flushed out with F-buffer (50 mM KCl, 2 mM $MgCl_2$, 20 mM imidazole). To prevent drying between flushing steps, the chamber was kept in a humid atmosphere.

SUV preparation

Lipids were stored in chloroform. To remove chloroform, lipid solution (typically 50 µl) was pipetted into a glass tube. Chloroform was slowly evaporated by gentle nitrogen flow while turning the tilted glass tube to achieve a homogenous layer of lipids at the bottom of the tube. To remove any remaining chloroform, the tube was kept in a vacuum overnight. The lipids were resuspended in buffer (20 mM imidazole, 50 mM KCl) and sonicated with a tip sonicator for 30 min to make SUVs. We used 1.9 mg/ml of the neutral lipid 1,2-dioleoyl-sn-glycero-3-phosphocholine (DOPC; Avanti Polar Lipids). For open chamber experiments, we supplemented the membrane with 1 mol% PEGylated lipids 1,2-dipalmitoyl-sn-glycero-3-phosphoethanolamine-N-[methoxy(polyethylene glycol)-2000] (PEG-PE; Avanti Polar Lipids) to make the bilayer more resilient against drying.

Contraction experiments

In the cases where we used an open chamber, actin was pre-polymerized for longer than 1 h. Myosin was then added with the contraction buffer [50 mM KCl, 2 mM $MgCl_2$, 20 mM imidazole, 1 mM DTT, 0.1 mM ATP, 2 mM protocatechuic acid (PCA), 0.1 µM protocatechuase 3,4-dioxygenase (PCD), 10 mM creatine phosphate, 0.1 mg/ml creatine kinase, 0.3% methyl cellulose (MC)]. Creatine phosphate and creatine kinase were used as an ATP-replenishing system, PCA and PCD were used as an oxygen-scavenger system to limit photobleaching, and MC acted as a crowding agent that pushes actin and myosin filaments towards the coverslip. In flow cell experiments, monomeric actin was mixed with the contraction buffer, which triggers its polymerization, and the mix was immediately injected into the channel. Exact actin and myosin concentrations for the experiments presented in the main text can be found in Table S1.

Diluted filament assay

Diluted filament conditions shown in Figs 2–4 were obtained either by polymerizing actin at low concentration or by slowing down the polymerization of an initially dense actin solution by diluting after a few minutes. The exact conditions can be found in Table S1. Myosin was added to the filaments in the contraction buffer. For experiments in which myosin activity was triggered by the addition of ATP to a final concentration of 0.1 mM (Fig. 2A), the contraction buffer initially did not contain ATP.

Microscopy and image analysis

Images were taken with a number of different microscopes (see Table S1). Confocal images were taken with a Nikon Eclipse Ti inverted microscope equipped with a Nikon C1 confocal scan head and a 100 mW Argon ion laser (488 nm, 561 nm; Coherent), a Plan Fluor 10×0.3 NA, an S Fluor 40×1.3 NA and an Apo TIRF 100×1.49 NA objective, or with a Nikon Eclipse Ti inverted microscope equipped with a CrEST spinning disk unit, a solid state light source (SpectraX, Lumencor), a Plan Fluor 10×0.3 NA objective and a Hamamatsu camera. The typical exposure time was 200 ms. TIRF imaging was performed with a Nikon Eclipse Ti-E inverted microscope equipped with a Roper TIRF module, a QuantEM:512SC EMCCD camera and an Apo TIRF 100×1.49 NA oil objective. The exposure time was 400 ms for CP and 100 ms for all other proteins.

Image analysis was performed with the ImageJ distribution Fiji (Schindelin et al., 2012). The background intensity was subtracted with Fiji. For representation purposes, images were smoothened with the Fiji 'smooth' function. The velocity of myosin filament motion on actin filaments (Figs 1C and 3B) was measured by manual tracking of single myosin filaments using the 'Manual Tracking' plugin of ImageJ (https://imagej.nih.gov/ij/plugins/track/track.html). Temporal overlays (Fig. 6; Fig. S5) were made with the ImageJ plugin 'Temporal-Color Coder' (https://zenodo.org/record/1447158#.XAZlS2j7QuV). Kymographs were made with Fiji. Myosin trajectories in Fig. 1C were measured after aster formation. To detect myosin and actin filament edges (Fig. 3), we took line profiles of the respective fluorescence signals. The edge position was determined as the maximum in the first derivative of the profiles.

Electron microscopy

Transmission electron microscopy images of myosin filaments were taken with an FEI Verios 460. Myosin was assembled at a myosin concentration of 0.2 µM in the same F-buffer that was used for contraction assays. The solution was diluted (typically 1:100), applied on an electron microscopy grid (300-mesh Cu grid, Ted Pella), and rinsed with ultrapure water after 1 min of incubation. Finally, the grid was air-dried. Myosin length measurements were performed manually with the ImageJ distribution Fiji (Schindelin et al., 2012).

Estimating the characteristic dwell-time

Assuming a first-order process, the probability $p(t)$ that myosin has detached from the actin filament at time t reads as follows:

$$p(t) = 1 - e^{-t/\tau}$$

where τ is the characteristic dwell time. Because 6% (P=0.06) of the myosin has detached at t=4 min, inverting this formula yields an estimate of $\tau \approx 64$ min.

Computer simulations

The simulations of contractile actin-myosin networks were performed with the Open Source software Cytosim (github.com/nedelec/cytosim), which uses a Brownian dynamics approach as described previously (Nédélec and Foethke, 2007) (Table S2). Actin filaments are modeled as incompressible bendable filaments of rigidity 0.075 pN µm^2 (corresponding to a persistence length of 18 µm) in a medium of viscosity 0.18 Pa. The crosslinkers are modeled as Hookean springs of zero resting length and a rigidity of 50 pN/µm, with a binding rate k_{on}=15 s^{-1}, a binding range of 0.02 µm and a slip-bond unbinding model $k_{off}=k_{off,0}\exp(-|f|/f_0)$, with a basal unbinding rate of $k_{off,0}$=0.3 s^{-1} and unbinding force f_0=1 pN. Myosin minifilaments are modeled as an inextensible 1D object of length 0.8 µm with four motors on each side spaced by 0.08 µm from the extremities. Motors operate independently from each other and behave as a Hookean spring when attached to an actin filament, with zero resting length and a rigidity of 100 pN/µm. Additionally, motors move on filaments with a speed of 2 µm/s, with a linear force-velocity relationship characterized by a stall force of 4 pN. Each motor has a binding rate of k_{on}=10 s^{-1}, a binding range of 0.01 µm and a force-independent unbinding rate of k_{off}=0.5 s^{-1}. Unless otherwise specified, motors end-dwell by stopping upon reaching the end of filaments without changing their unbinding rates. Motors and crosslinker binding and unbinding events were modeled as first-order stochastic processes, and we neglected steric interaction between filaments, motors and crosslinkers.

The simulations without crosslinkers (Fig. 7A,B) were performed with 200 actin filaments randomly distributed over a square area of 40×40 μm^2, with filament lengths following an exponential distribution, with a mean length of 10 μm that was truncated inside [0.5; 20] μm. For the simulations reproducing the *in vitro*-like conditions (Fig. 7C,D), 800 actin filaments were randomly distributed over a square area of 80×80 μm^2, with filament lengths distribution as before. In those simulations, the resulting mesh size (measured as the average distance between consecutive filament crossings) was ∼1.1 μm. For the simulations that reproduce the cortex-like conditions, 3500 filaments were randomly distributed over a square area of 8×8 μm^2, with exponentially distributed lengths, with a mean of 1 μm truncated in [0.1; 4] μm. The resulting mesh size was ∼0.1 μm. In both scenarios, the actin filaments are mixed with varying amounts of crosslinkers and myosin minifilaments. The concentrations of myosin and crosslinkers are defined as number of elements per total length of actin (units of μm^{-1}) and varied within the ranges [0.1; 3.2 μm^{-1}] and [2; 64 μm^{-1}], respectively, for both scenarios. To better mimic experimental conditions, actin filaments are not created as straight filaments, but already relaxed according to their persistence length (18 μm), and the simulations start with all motors and crosslinkers unbound. The reference configuration files for each scenario are available to download from http://www.cytosim.org/publications/Wollrab2018/configs.zip.

In the phase diagrams (Figs 7D,E and 8A,B), the boundary between regions dominated by the polarity-sorting (PS) versus filament-buckling (FB) mechanisms was estimated by comparing the contraction rates of networks with and without end-dwelling. The contraction rates were calculated as in Belmonte et al. (2017). The regions of the phase diagram in which 50% or more of the contraction (see below) is lost when end-dwelling is disabled were considered to be dominated by the PS mechanism. The boundary line is estimated by creating a matrix with the normalized difference in contraction between the simulations with and without end-dwelling, which was later smoothed using a 2D boxcar average with a window size of 3. We then used the matplotlib library from Python to calculate the isocline at 0.5. The networks that experience a small initial contraction (10% or less) that stopped after a few seconds were considered to be noncontractile and labeled as the stalled (S) region of the phase diagrams in Fig. 8. Note that the networks in the same region of the phase diagrams in Fig. 7 experience a slow, but continuous, contraction and therefore were not considered stalled.

Estimation of the contractility in simulations

The center of the network is the average of all the vertices used to model the filaments: $c = (1/P)\sum x_i$, where P is the total number of vertices in the system. An effective radius of the network is calculated as:

$$R = \sqrt{\frac{2}{P}\sum_i (x_i - c)^2}.$$

The contraction is 10% when R reaches 0.9 R_0. The (negative) expansion rate is estimated by finite difference: $((dR)/(dt))(t)=[R(t+\tau)-R(t)]/\tau$.

Simulation files

All simulation configuration files used to generate Figs 7 and 8 and Movies 10–15 are available at http://www.cytosim.org/publications/Wollrab2018/configs.zip. The files with extension 'cym' are text files containing the description of the model. These files are input to the freely available simulation software Cytosim (https://github.com/nedelec/cytosim). The files with extension 'cym.tpl' are templates that can be expanded using preconfig (Nedelec, 2017) available at https://github.com/nedelec/preconfig. Note that because the filament lengths are truncated, we used a higher value in the filament exponential distribution instruction in the configuration files in order to obtain an actual average filament length close to 10 μm or 1 μm.

Acknowledgements

We thank Dr C. Le Clainche [Institute for Integrative Biology of the Cell (I2BC), Université Paris-Sud] for kindly providing the α-actinin-1 constructs and protein purification protocol; Dr D. Kovar and Dr Cristian Suarez (University of Chicago) for the kind gift of the SNAP-CP construct and protein purification protocol; and Marjolein Vinkenoog-Kuit and Jeffrey den Haan for protein purification. We acknowledge European Molecular Biology Laboratory IT support.

Competing interests

The authors declare no competing or financial interests.

Author contributions

Conceptualization: V.W., J.M.B., M.L., G.H.K.; Methodology: V.W., J.M.B., F.N., G.H.K.; Software: J.M.B., F.N.; Validation: V.W., F.N., G.H.K.; Formal analysis: V.W., J.M.B., F.N.; Investigation: V.W., J.M.B., L.B.; Data curation: V.W.; Writing - original draft: V.W., J.M.B., G.H.K.; Writing - review & editing: V.W., J.M.B., L.B., M.L., F.N., G.H.K.; Visualization: V.W., J.M.B., L.B.; Supervision: M.L., F.N., G.H.K.; Project administration: V.W., G.H.K.; Funding acquisition: M.L., G.H.K.

Funding

This work was supported by the Center for Modelling and Simulation in the Biosciences (F.N.), the European Research Council [335672-MINICELL], the European Molecular Biology Laboratory (F.N., J.M.B., M.L.), the European Molecular Biology Organization (J.M.B., M.L.) and H2020 Marie Skłodowska-Curie Actions.

Data availability

The configuration files used for Cytosim software are available from http://www.cytosim.org/publications/Wollrab2018/configs.zip, or from the corresponding authors on request.

Supplementary information

Supplementary information available online at http://jcs.biologists.org/lookup/doi/10.1242/jcs.219717.supplemental

References

Akhmanova, A. and Hoogenraad, C. C. (2005). Microtubule plus-end-tracking proteins: Mechanisms and functions. *Curr. Opin. Cell Biol.* **17**, 47-54.

Alvarado, J. and Koenderink, G. H. (2015). Reconstituting cytoskeletal contraction events with biomimetic actin e myosin active gels. *Methods Cell Biol.* **128**, 83-103.

Alvarado, J., Sheinman, M., Sharma, A., MacKintosh, F. C. and Koenderink, G. H. (2013). Molecular motors robustly drive active gels to a critically connected state. *Nat. Phys.* **9**, 591-597.

Alvarado, J., Sheinman, M., Sharma, A., MacKintosh, F. C. and Koenderink, G. H. (2017). Force percolation of contractile active gels. *Soft Mat.* **13**, 5624-5644.

Backouche, F., Haviv, L., Groswasser, D. and Bernheim-Groswasser, A. (2006). Active gels: dynamics of patterning and self-organization. *Phys. Biol.* **3**, 264-273.

Begg, D. A., Rodewald, R. and Rebhun, L. I. (1978). The Visualization of actin filaments in thin sections. *J. Cell Biol.* **79**, 846-852.

Belmonte, J. M., Leptin, M. and Nédélec, F. (2017). A theory that predicts behaviors of disordered cytoskeletal networks. *Mol. Syst. Biol.* **13**, 941.

Bendix, P. M., Koenderink, G. H., Cuvelier, D., Dogic, Z., Koeleman, B. N., Brieher, W. M., Field, C. M., Mahadevan, L. and Weitz, D. A. (2008). A quantitative analysis of contractility in active cytoskeletal protein networks. *Biophys. J.* **94**, 3126-3136.

Billington, N., Wang, A., Mao, J., Adelstein, R. S. and Sellers, J. R. (2013). Characterization of three full-length human nonmuscle myosin II paralogs. *J. Biol. Chem.* **288**, 33398-33410.

Biro, M., Romeo, Y., Kroschwald, S., Bovellan, M., Boden, A., Tcherkezian, J., Roux, P. P., Charras, G. and Paluch, E. K. (2013). Cell cortex composition and homeostasis resolved by integrating proteomics and quantitative imaging. *Cytoskeleton* **70**, 741-754.

Blanchoin, L., Boujemaa-paterski, R., Sykes, C. and Plastino, J. (2014). Actin dynamics, architecture, and mechanics in cell motility. *Physiol. Rev.* **94**, 235-263.

Bovellan, M., Romeo, Y., Biro, M., Boden, A., Chugh, P., Yonis, A., Vaghela, M., Fritzsche, M., Moulding, D., Thorogate, R. et al. (2014). Cellular control of cortical actin nucleation. *Curr. Biol.* **24**, 1628-1635.

Bun, P., Dmitrieff, S., Belmonte, J. M., Nédélec, F. and Lénart, P. (2018). A disassembly-driven mechanism explains F-actin-mediated chromosome transport in starfish oocytes. *eLife* **7**, e31469.

Burke, T. A., Harker, A. J., Dominguez, R. and Kovar, D. R. (2017). The bacterial virulence factors VopL and VopF nucleate actin from the pointed end. *J. Cell Biol.* **216**, 1267-1276.

Chalut, K. J. and Paluch, E. K. (2016). Forum the actin cortex: a bridge between cell shape and function. *Dev. Cell.* **38**, 571-573.

Chugh, P. and Paluch, E. K. (2018). The actin cortex at a glance. *J. Cell Sci.* **131**, 1-9.

Chugh, P., Clark, A. G., Smith, M. B., Cassani, D. A. D., Dierkes, K., Ragab, A., Roux, P. P., Charras, G., Salbreux, G. and Paluch, E. K. (2017). Actin cortex architecture regulates cell surface tension. *Nat. Cell Biol.* **19**, 689-697.

Ciobanasu, C., Faivre, B. and Le Clainche, C. (2014). Actomyosin-dependent formation of the mechanosensitive talin-vinculin complex reinforces actin anchoring. *Nat. Commun.* **5**, 3095.
Cramer, L. P., Siebert, M. and Mitchison, T. J. (1997). Identification of novel graded polarity actin filament bundles in locomoting heart fibroblasts: Implications for the generation of motile force. *J. Cell Biol.* **136**, 1287-1305.
Dasanayake, N. L., Michalski, P. J. and Carlsson, A. E. (2011). General mechanism of actomyosin contractility. *Phys. Rev. Lett.* **107**, 118101.
Ding, W. Y., Ong, H. T., Hara, Y., Wongsantichon, J., Toyama, Y., Robinson, R. C., Nédélec, F. and Bar, R. Z. (2017). Plastin increases cortical connectivity to facilitate robust polarization and timely cytokinesis. *J. Cell Biol.* **216**, 1371-1386.
Eghiaian, F., Rigato, A. and Scheuring, S. (2015). Structural, mechanical, and dynamical variability of the actin cortex in living cells. *Biophys. J.* **108**, 1330-1340.
Ennomani, H., Letort, G., Guérin, C., Martiel, J.-L., Cao, W., Nédélec, F., De La Cruz, E. M., Théry, M. and Blanchoin, L. (2016). Architecture and connectivity govern actin network contractility. *Curr. Biol.* **26**, 616-626.
Erdmann, T., Bartelheimer, K. and Schwarz, U. S. (2016). Sensitivity of small myosin II ensembles from different isoforms to mechanical load and ATP concentration. *Phys. Rev. E - Stat. Nonlinear, Soft Matter Phys.* **94**, 052403.
Field, C. M. and Lénárt, P. (2011). Bulk cytoplasmic actin and its functions in meiosis and mitosis. *Curr. Biol.* **21**, 825-830.
Foster, P. J., Furthauer, S., Shelley, M. J. and Needleman, D. J. (2015). Active contraction of microtubule networks. *eLife* **4**, e10837.
Freedman, S. L., Banerjee, S., Hocky, G. M. and Dinner, A. R. (2017). A versatile framework for simulating the dynamic mechanical structure of cytoskeletal networks. *Biophys. J.* **113**, 448-460.
Freedman, S. L., Hocky, G. M., Banerjee, S. and Dinner, A. R. (2018). Nonequilibrium phase diagrams for actomyosin networks. *Soft Mat.* **14**, 7740-7747.
Fritzsche, M., Erlenkämper, C., Moeendarbary, E., Charras, G. and Kruse, K. (2016). Actin kinetics shapes cortical network structure and mechanics. *Sci. Adv.* **2**, e1501337.
Fritzsche, M., Li, D., Colin-York, H., Chang, V. T., Moeendarbary, E., Felce, J. H., Sezgin, E., Charras, G., Betzig, E. and Eggeling, C. (2017). Self-organizing actin patterns shape membrane architecture but not cell mechanics. *Nat. Commun.* **8**, 14347.
Fujiwara, T. K., Iwasawa, K., Kalay, Z., Tsunoyama, T. A., Watanabe, Y., Umemura, Y. M., Murakoshi, H., Suzuki, K. G. N., Nemoto, Y. L., Morone, N. et al. (2016). Confined diffusion of transmembrane proteins and lipids induced by the same actin meshwork lining the plasma membrane. *Mol. Biol. Cell* **27**, 1101-1119.
Gautel, M. and Djinović-Carugo, K. (2016). The sarcomeric cytoskeleton: from molecules to motion. *J. Exp. Biol.* **219**, 135-145.
Guthardt Torres, P., Doubrovinski, K. and Kruse, K. (2010). Filament turnover stabilizes contractile cytoskeletal structures. *Europhys. Lett.* **91**, 68003.
Hannezo, E., Dong, B., Recho, P., Joanny, J.-F. and Hayashi, S. (2015). Cortical instability drives periodic supracellular actin pattern formation in epithelial tubes. *Proc. Natl. Acad. Sci.* **112**, 8620-8625.
Harris, D. E. and Warshaw, D. M. (1993). Smooth and skeletal muscle myosin both exhibit low duty cycles at zero load in vitro. *J. Biol. Chem.* **268**, 14764-14768.
Houdusse, A. and Sweeney, H. L. (2016). How myosin generates force on actin filaments. *Trends Biochem. Sci.* **41**, 989-997.
Hu, S., Dasbiswas, K., Guo, Z., Tee, Y.-H., Thiagarajan, V., Hersen, P., Chew, T.-L., Safran, S. A., Zaidel-Bar, R. and Bershadsky, A. D. (2017). Long-range self-organization of cytoskeletal myosin II filament stacks. *Nat. Cell Biol.* **19**, 133.
Jégou, A. and Romet-Lemonne, G. (2016). Perspective single filaments to reveal the multiple flavors of actin. *Biophys. J.* **110**, 2138-2146.
Jülicher, F., Kruse, K., Prost, J. and Joanny, J.-F. (2007). Active behavior of the cytoskeleton. *Phys. Rep.* **449**, 3-28.
Kamasaki, T., Osumi, M. and Mabuchi, I. (2007). Three-dimensional arrangement of F-actin in the contractile ring of fission yeast. *J. Cell Biol.* **178**, 765-771.
Kang, H., Bradley, M. J., McCullough, B. R., Pierre, A., Grintsevich, E. E., Reisler, E. and De La Cruz, E. M. (2012). Identification of cation-binding sites on actin that drive polymerization and modulate bending stiffness. *PNAS* **109**, 16923-16927.
Koenderink, G. H. and Paluch, E. K. (2018). Architecture shapes contractility in actomyosin networks. *Curr. Opin. Cell Biol.* **50**, 79-85.
Koenderink, G. H., Dogic, Z., Nakamura, F., Bendix, P. M., MacKintosh, F. C., Hartwig, J. H., Stossel, T. P. and Weitz, D. A. (2009). An active biopolymer network controlled by molecular motors. *Proc. Natl. Acad. Sci.* **106**, 15192-15197.
Köhler, S., Schaller, V. and Bausch, A. R. (2011). Structure formation in active networks. *Nat. Mater.* **10**, 462-468.
Köster, D. V., Husain, K., Iljazi, E., Bhat, A., Bieling, P., Mullins, R. D., Rao, M. and Mayor, S. (2016). Actomyosin dynamics drive local membrane component organization in an in vitro active composite layer. *Proc. Natl. Acad. Sci.* **113**, E1645-E1654.
Kovács, M., Wang, F., Hu, A., Zhang, Y. and Sellers, J. R. (2003). Functional divergence of human cytoplasmic myosin II. Kinetic characterization of the non-muscle IIA isoform. *J. Biol. Chem.* **278**, 38132-38140.
Kruse, K. and Jülicher, F. (2000). Actively contracting bundles of polar filaments. *Phys. Rev. Lett.* **85**, 1778-1781.
Lenz, M. (2014). Geometrical origins of contractility in disordered actomyosin networks. *Phys. Rev. X* **4**, 1-9.
Lenz, M., Thoresen, T., Gardel, M. L. and Dinner, A. R. (2012). Contractile units in disordered actomyosin bundles arise from f-actin buckling. *Phys. Rev. Lett.* **108**, 238107.
Li, J., Biel, T., Lomada, P., Yu, Q. and Kim, T. (2018). Buckling-induced F-actin fragmentation modulates contraction of active cytoskeletal networks. *Soft* **13**, 3213-3220.
Linsmeier, I., Banerjee, S., Oakes, P. W., Jung, W., Kim, T. and Murrell, M. P. (2016). Disordered actomyosin networks are sufficient to produce cooperative and telescopic contractility. *Nat. Commun.* **7**, 12615.
Liu, X., Shu, S. and Korn, E. D. (2018). Polymerization pathway of mammalian nonmuscle myosin 2s. *Proc. Natl. Acad.* **115**, E7101-E7108.
Lu, W., Fox, P., Lakonishok, M., Davidson, M. W. and Gelfand, V. I. (2013). Initial neurite outgrowth in Drosophila neurons is driven by kinesin-powered microtubule sliding. *Curr. Biol.* **23**, 1018-1023.
Luo, W., Yu, C.-H., Lieu, Z. Z., Allard, J., Mogilner, A., Sheetz, M. P. and Bershadsky, A. D. (2013). Analysis of the local organization and dynamics of cellular actin networks. *J. Cell Biol.* **202**, 1057-1073.
MacKintosh, F. C. and Levine, A. J. (2008). Nonequilibrium mechanics and dynamics of motor-activated gels. *Phys. Rev. Lett.* **100**, 018104.
Martin, A. C., Kaschube, M. and Wieschaus, E. F. (2009). Pulsed contractions of an actin-myosin network drive apical constriction. *Nature* **457**, 495-499.
Mayer, M., Depken, M., Bois, J. S., Jülicher, F. and Grill, S. W. (2010). Anisotropies in cortical tension reveal the physical basis of polarizing cortical flows. *Nature* **467**, 617-621.
McFadden, W. M., McCall, P. M., Gardel, M. L. and Munro, E. M. (2017). Filament turnover tunes both force generation and dissipation to control long- range flows in a model actomyosin cortex. *PLoS Comput. Biol.* **13**, e1005811.
Melli, L., Billington, N., Sun, S. A., Bird, J., Nagy, A., Friedman, T. B., Takagi, Y. and Sellers, J. R. (2017). Bipolar filaments of human nonmuscle myosin 2-A and 2-B have distinct motile and mechanical properties. *eLife* **7**, e32871.
Mendes Pinto, I., Rubinstein, B., Kucharavy, A., Unruh, J. R. and Li, R. (2012). Actin depolymerization drives actomyosin ring contraction during budding yeast cytokinesis. *Dev. Cell* **22**, 1247-1260.
Munjal, A., Philippe, J.-M., Munro, E. and Lecuit, T. (2015). A self-organized biomechanical network drives shape changes during tissue morphogenesis. *Nature* **524**, 351-355.
Murrell, M. P. and Gardel, M. L. (2012). F-actin buckling coordinates contractility and severing in a biomimetic actomyosin cortex. *Proc. Natl. Acad. Sci. USA* **109**, 20820-20825.
Murrell, M. and Gardel, M. L. (2014). Actomyosin sliding is attenuated in contractile biomimetic cortices. *Mol. Biol. Cell* **25**, 1845-1853.
Murrell, M., Oakes, P. W., Lenz, M. and Gardel, M. L. (2015). Forcing cells into shape: the mechanics of actomyosin contractility. *Nat. Rev. Mol. Cell Biol.* **16**, 486-498.
Naumanen, P., Lappalainen, P. and Hotulainen, P. (2008). Mechanisms of actin stress fibre assembly. *J. Microsc.* **231**, 446-454.
Nedelec, F. (2017). preconfig: a versatile configuration file generator for varying parameters. *J. Open Res. Softw.* **5**, 1-4.
Nédélec, F. and Foethke, D. (2007). Collective Langevin dynamics of flexible cytoskeletal fibers. *New J. Phys.* **9**, 427.
Nédélec, F. J., Surrey, T., Maggs, A. C. and Leibler, S. (1997). Self-organization of microtubules and motors. *Nature* **389**, 305-308.
Nishikawa, M., Naganathan, S. R., Jülicher, F. and Grill, S. W. (2017). Controlling contractile instabilities in the actomyosin cortex. *eLife* **6**, 1-21.
Ronceray, P., Broedersz, C. P. and Lenz, M. (2016). Fiber networks amplify active stress. *Proc. Natl. Acad. Sci.* **113**, 2827-2832.
Rubinstein, B. Y. and Mogilner, A. (2017). Myosin clusters of finite size develop contractile stress in 1d random actin arrays. *Biophysj* **113**, 937-947.
Salbreux, G., Prost, J. and Joanny, J.-F. (2009). Hydrodynamics of cellular cortical flows and the formation of contractile rings. *Phys. Rev. Lett.* **103**, 058102.
Sanchez, T., Chen, D. T. N., DeCamp, S. J., Heymann, M. and Dogic, Z. (2012). Spontaneous motion in hierarchically assembled active matter. *Nature* **491**, 431-434.
Sanger, J. M. and Sanger, J. W. (1980). Banding and polarity of actin filaments in interphase and cleaving cells. *J. Cell Biol.* **86**, 568-575.
Schindelin, J., Arganda-Carreras, I., Frise, E., Kaynig, V., Longair, M., Pietzsch, T., Preibisch, S., Rueden, C., Saalfeld, S., Schmid, B. et al. (2012). Fiji: an open-source platform for biological-image analysis. *Nat. Methods* **9**, 676-682.
Schneider, C. A., Rasband, W. S. and Eliceiri, K. W. (2012). NIH Image to ImageJ: 25 years of image analysis. *Nat. Methods* **9**, 671-675.
Schuppler, M., Keber, F. C., Kröger, M. and Bausch, A. R. (2016). Boundaries steer the contraction of active gels. *Nat. Commun.* **7**, 13120.
Sellers, J. R. and Kachar, B. (1990). Polarity and velocity of sliding filaments: control of direction by actin and of speed by myosin. *Science* **249**, 406-408.

Sharma, A., Licup, A. J., Jansen, K. A., Rens, R., Sheinman, M., Koenderink, G. H. and MacKintosh, F. C. (2016). Strain-controlled criticality governs the nonlinear mechanics of fibre networks. *Nat. Phys.* 12, 584-587.

Sheinman, M., Sharma, A., Alvarado, J., Koenderink, G. H. and Mackintosh, F. C. (2015). Anomalous discontinuity at the percolation critical point of active gels. *Phys. Rev. Lett.* **114**, 098104.

Soares e Silva, M., Depken, M., Stuhrmann, B., Korsten, M., MacKintosh, F. C. and Koenderink, G. H. (2011). Active multistage coarsening of actin networks driven by myosin motors. *Proc. Natl. Acad. Sci.* **108**, 9408-9413.

Stam, S., Freedman, S. L., Banerjee, S., Weirich, K. L., Dinner, A. R. and Gardel, M. L. (2017). Filament rigidity and connectivity tune the deformation modes of active biopolymer networks. *Proc. Natl. Acad. Sci.* **114**, E10037-E10045.

Surrey, T., Nédélec, F., Leibler, S. and Karsenti, E. (2001). Physical properties determining self-organization of motors and microtubules. *Science (80-.).* **292**, 1167-1171.

Tan, R., Foster, P. J., Needleman, D. J. and McKenney, R. J. (2018). Cooperative accumulation of dynein-dynactin at microtubule minus-ends drives microtubule network reorganization. *Dev. Cell.* **44**, 233-247.

Thoresen, T., Lenz, M. and Gardel, M. L. (2013). Thick filament length and isoform composition determine self-organized contractile units in actomyosin bundles. *Biophys. J.* **104**, 655-665.

Torisawa, T., Taniguchi, D., Ishihara, S. and Oiwa, K. (2016). Spontaneous formation of a globally connected contractile network in a microtubule-motor system. *Biophys. J.* **111**, 373-385.

Vavylonis, D., Wu, J.-Q., Hao, S., O'Shaughnessy, B. and Pollard, T. D. (2008). Assembly mechanism of the contractile ring for cytokinesis by fission yeast. *Science (80-.)* **319**, 97-100.

Verkhovsky, A. B., Svitkina, T. M. and Borisy, G. G. (1997). Polarity sorting of actin filaments in cytochalasin-treated fibroblasts. *J. Cell Sci.* **1704**, 1693-1704.

Vogel, S. K., Petrasek, Z., Heinemann, F. and Schwille, P. (2013). Myosin motors fragment and compact membrane-bound actin filaments. *eLife* **2**, e00116.

Wang, F., Kovács, M., Hu, A., Limouze, J., Harvey, E. V. and Sellers, J. R. (2003). Kinetic mechanism of non-muscle myosin IIB: functional adaptations for tension generation and maintenance. *J. Biol. Chem.* **278**, 27439-27448.

Wehland, J., Osborn, M. and Weber, K. (1977). Phalloidin-induced actin polymerization in the cytoplasm of cultured cells interferes with cell locomotion and growth. *Proc. Natl. Acad.* **74**, 5613-5617.

Wollrab, V., Thiagarajan, R., Wald, A., Kruse, K. and Riveline, D. (2016). Still and rotating myosin clusters determine cytokinetic ring constriction. *Nat. Commun.* **7**, 11860.

Yamada, A. and Wakabayashi, T. (1993). Movement of actin away from the center of reconstituted rabbit myosin filament is slower than in the opposite direction. *Biophys. J.* **64**, 565-569.

Zaidel-Bar, R., Zhenhuan, G. and Luxenburg, C. (2015). The contractome - a systems view of actomyosin contractility in non-muscle cells. *J. Cell Sci.* **128**, 2209-2217.

Zumdieck, A., Kruse, K., Bringmann, H., Hyman, A. A. and Jülicher, F. (2007). Stress generation and filament turnover during actin ring constriction. *PLoS ONE* **2**, e696.